Effect of hydrothermal temperature on the photocatalytic activity of anatase TiO$_2$ nanoparticles

Malligavathy Rajakumar*, Pathinettam Padiyan

Abstract
We report the significance of hydrothermal temperature of TiO$_2$ nanoparticles on the crystallinity, band gap and the photocatalytic degradation of congo red dye. These nanoparticles are synthesized by hydrothermal method at 120 ^oC, 140 ^oC and 160 ^oC. The anatase phases of the samples are confirmed from the X-ray diffraction pattern and the surface morphology of the sample is visualized in a high-resolution scanning electron microscope. The observed optical band gap value supported that TiO$_2$ can be used as a visible light photocatalyst which is also in agreement with the photoluminescence spectrum. TiO$_2$ nanoparticles prepared at 160 ^oC degrades 98.3 % of congo red in 90 min and the kinetics of degradation is analysed using both pseudo first (Langmuir Hinshelwood) and second order equations. It is found that the pseudo second order (Blanchard) equation fits well for the whole range of degradation with the correlation coefficient of 0.9999.

Keywords
Titanium dioxide, Hydrothermal method, Photocatalytic degradation, Congo red.

Department of Physics, Manonmaniam Sundaranar University, Tirunelveli-627 012, Tamil Nadu, India.
***Corresponding author**: malligavathy2017@gmail.com

1. Introduction

Semiconductor photocatalyst are mainly preferred for the dye waste water treatment because it is inexpensive and low toxicity. Among various metal oxide semiconductors, Titanium dioxide (TiO$_2$) is known to be an important semiconductor material attracts tremendous attention due to its wide range of applications including photocatalytic degradation [1], photovoltaic devices, solar cells, gas sensor and humidity sensors. It is well known that titanium dioxide exists in three crystalline polymorphs namely anatase, rutile and brookite. Among these, anatase phase has a higher photocatalytic activity in comparison with rutile phase because of its lower electron-hole recombination rate. Various synthetic methods such as hydrothermal [2], solvothermal [3] and sol–gel method [4] have been used for the preparation of TiO$_2$ nanoparticles. Among these preparation routes, hydrothermal synthesis is a promising method because it provides an effective environment for the synthesis of nanocrystalline TiO$_2$ with high purity, good dispersion and well-controlled crystalline. Hong-xu Guo et.al [5] prepared TiO$_2$ nanoparticles by hydrothermal method at the temperature of 160 ^oC for 10 h and studied its photocatalytic degradation of congo red (CR) with a concentration of 40 ppm. They used 1.5 g/l of catalyst in 100 ml of dye solution and achieved 12 % efficiency in 210 min. Mansoor Farbod et.al [6] prepared TiO$_2$ nanoparticles using sol-gel ball milling method which degraded 80 % of CR (20 ppm) in 210 min irradiation using 1 g/l catalyst. M.L. de Souza et.al [7] reported 80 % of CR (20 ppm) degradation in 240 min using 0.5 g/l photocatalyst. The aim of the present

work is to prepare anatase phase TiO$_2$ nanoparticles with higher degradation property of the congo red dye.

2. Experimental details

2.1 Materials used

Titanium (IV) isopropoxide (Sigma Aldrich), ethanol, glacial acetic acid (Merck) and congo red (Sigma Aldrich) were purchased and used for the sample preparation. Double distilled (DD) water was used throughout the experiment.

2.2 Preparation

TiO$_2$ nanoparticles were prepared by hydrothermal treatment using Titanium (IV) isopropoxide as a precursor. To the 5 ml of precursor, 10 ml of ethanol and 20 ml of double distilled water was added drop wise and stirred for 30 min. Then 5 ml of glacial acetic acid was added to the above solution (pH = 3). Now the resulting solution was transferred into a 50 ml Teflon-lined stainless-steel autoclave and hydrothermally treated at 120 ^oC in an oven for 24 h. Finally, the autoclave was cooled to room temperature, the precipitates were centrifuged and washed several times using double distilled water. The resulting precipitates were dried overnight in an oven at 80 ^oC and the sample was named as S$_1$. Similarly, the samples were hydrothermally treated at different temperatures 140 ^oC and 160 ^oC for 24 h and named as S$_2$ and S$_3$ respectively [8].

2.3 Characterization

X-ray diffraction was performed using PANalytical XPERT-PRO X-ray diffractometer with CuK$_\alpha$ (λ = 1.5406 Å) as
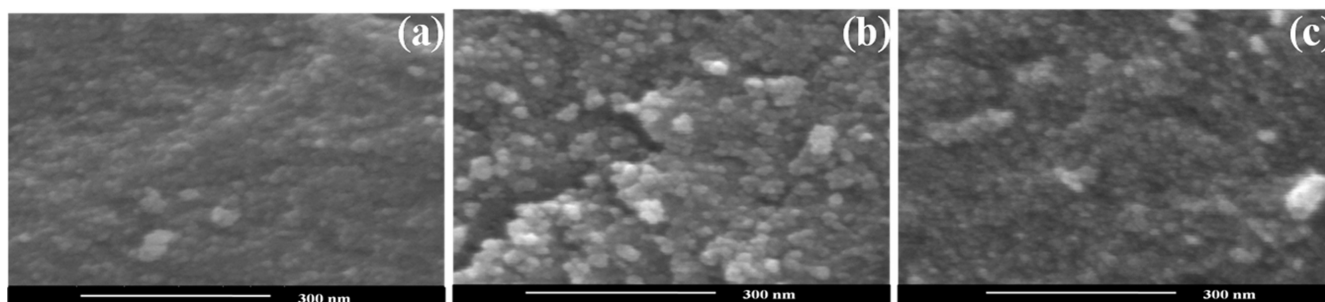
Figure 1. HR-SEM micrograph for TiO$_2$ nanoparticles of (a) S$_1$ (b) S$_2$ and (c) S$_3$

an incident radiation. The accelerating voltage and current were 40 kV and 30 mA respectively. The surface morphology and composition of the nanoparticles were observed in a High-Resolution Scanning Electron Microscope (FEI Quanta FEG 200) equipped with an Energy Dispersive X-ray spectroscopy (EDX). Transmission electron microscope (TEM) images were obtained using a Philips CM 200 at an accelerating voltage of 200 kV. The diameter of the TiO$_2$ nanoparticles was determined using the Image J software. After measuring the diameters, the data was represented in the form of a histogram in order to analyze the size distribution. Shimadzu UV-2700 diffuse reflectance spectrophotometer (DRS) was used to obtain reflectance and absorption spectra in the wavelength region 220-850 nm using BaSO$_4$ powder as reference. Photoluminescence (PL) spectra were obtained using Cary Eclips EL08083851 Fluorescence Spectrophotometer with an excitation wavelength of 388 nm. Congo Red (CR) was chosen as a model pollutant for degradation studies using TiO$_2$ as a catalyst. 500 W xenon source (Wacom XDS 501S) with a dimension of 160(W)×145(D)×377(H) mm was used for light irradiation (64,200 lx; wavelength: 220-2000 nm) and the distance between the light source and sample was kept as 47 cm. The degradation of CR dye of 10 ppm concentration was studied for every 30 min using TiO$_2$ nanoparticles (0.2 g/l) and the residual concentration of the dye in the solution was obtained using UV-Vis spectrophotometer (Techcomp, UV 2301) in the range of 200-900 nm.

3. Results

3.1 Structural properties

Figure 1 shows the HR-SEM image of TiO$_2$ nanoparticles prepared for various hydrothermal temperatures. From the figure, it is clear that smooth spherical particles are seen on the surface. The distribution of the particles is uniform and the particle size lies between 14-19 nm. With an increase in hydrothermal temperature, the samples possess well defined shapes and larger particle size. The EDX analysis indicated the presence of Ti and O in the TiO$_2$ nanoparticles. No other impurity peaks are observed in EDX confirming the purity of the sample.

Figure 2 (a), (b) and (c) shows the TEM image of the TiO$_2$ nanoparticles prepared at the hydrothermal temperature of 120 ^{o}C, 140 ^{o}C and 160 ^{o}C in which the nanoparticles show very similar shapes of rice grains with well monodispersed particles. Additionally, the agglomeration is absent in the samples and the images demonstrates the formation of crystalline TiO$_2$ with a particle size of about 14 to 19 nm. The particle size distributions for TiO$_2$ nanoparticles were estimated from TEM images and are given in figure 3. It can be seen that the particles are uniform in shape and have a particle size distribution in the range of 14–19 nm. The results of the particle size distribution of TiO$_2$ nanoparticles show an inter correlation with TEM and SEM results.

3.2 Optical properties

The optical absorbance spectra of TiO$_2$ nanoparticles synthesized at various temperatures are shown in figure 4. The peak around 300 nm is due to the charge transfer from O 2p orbital of the valence band to the conduction band of the Ti 3d orbital. Compared with other samples, sample S$_3$ shows strong absorption. Furthermore, the band edge shifts towards the higher wavelength, indicating a decrease in the band gap energy and consequently more photogenerated electrons and holes could participate in the photocatalytic reactions. The optical band gaps are calculated using Kubelka-Munk function [9]

$$F(R_\infty) = \frac{(1-R_\infty)^2}{2R_\infty} \tag{1}$$

The optical band gaps are obtained from the intercept of extrapolated linear fit of experimental data by a plot of $[F(R_\infty)h\nu]^{1/2}$ versus incident photon energy and is shown in figure 4 as an inset. The band gap values are found to be 3.176 (2), 3.064 (2) and 3.023 (5) eV for S$_1$, S$_2$ and S$_3$ samples respectively. The oxygen vacancy generated from the replacement of Ti^{4+} by Ti^{3+} in the TiO$_2$ lattice forms the impurity level above the valence band and it narrows the band gap of the sample [10]. The decreases in band gap values are well consistent with the XRD results of larger crystallite size and crystallinity.

Figure 5 shows the PL spectra of TiO$_2$ nanoparticles for various hydrothermal temperatures at an excitation wavelength of 388 nm recorded at room temperature. The intensity PL peaks can be linked to the recombination process of electron-hole pair at the surface of TiO$_2$ [11]. Commonly, PL emission of anatase TiO$_2$ is assigned to three different physical origins: self-trapped excitons, oxygen vacancies and surface
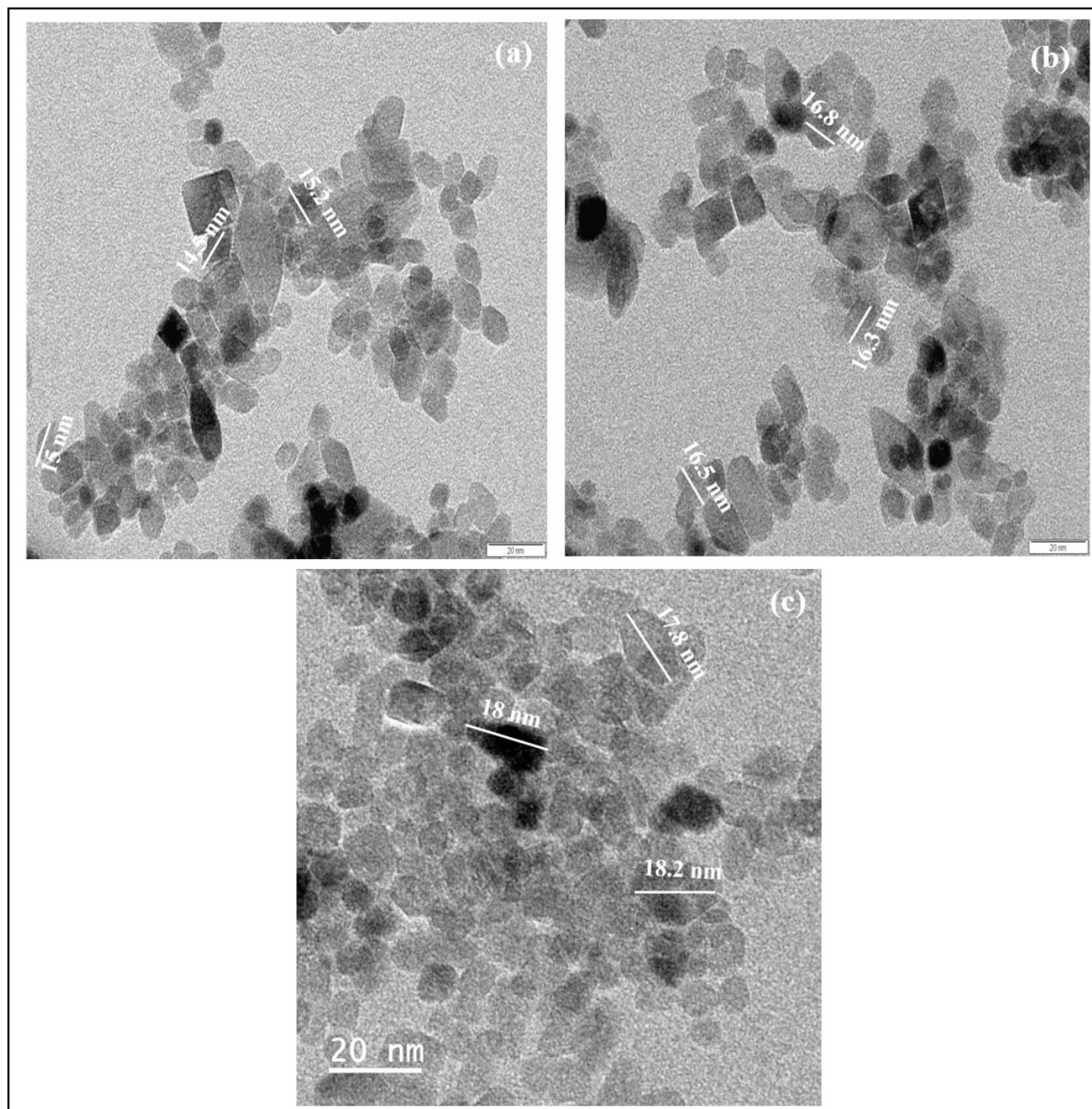
Figure 2. TEM micrograph for TiO_2 nanoparticles of (a) S_1 (b) S_2 and (c) S_3

defects [12]. The emission peaks ranging from 440 nm to 500 nm are due to the surface oxygen vacancies, impurities, defects [13] and transition of Ti-OH groups suggesting the existence of hydroxyl groups on the surface of TiO_2 nanoparticles [14]. There are six emission peaks observed in the visible region at 445, 459, 485, 517, 529 and 542 nm. The blue emissions at 445 and 459 nm are attributed to band edge free excitons [15] and shallow trap states. The green emissions at 485, 517, 529 and 542 nm are due to the trapping of free excitons by titanate groups near defects [16], radiative recombination of charge carriers and arise from the deep hole trap states associated with oxygen vacancies respectively. The increase in hydrothermal temperature increases the PL intensity which means that the crystallinity [17] and the photocatalytic activity [18] of TiO_2 increase at higher temperature. Thus the PL and DRS results explain the changes in the band gap of TiO_2 nanoparticles.
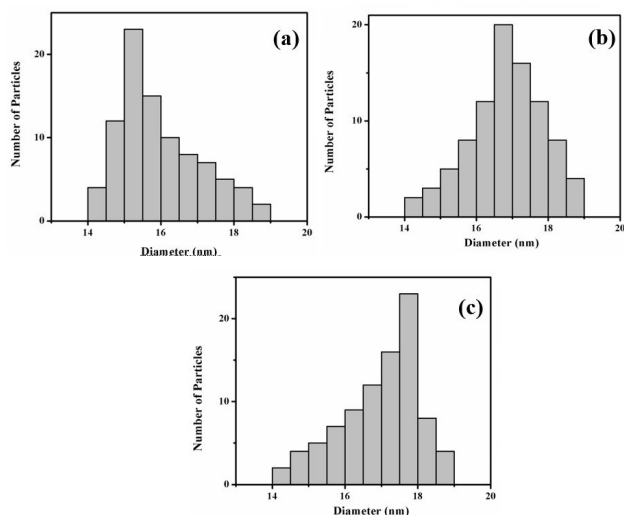
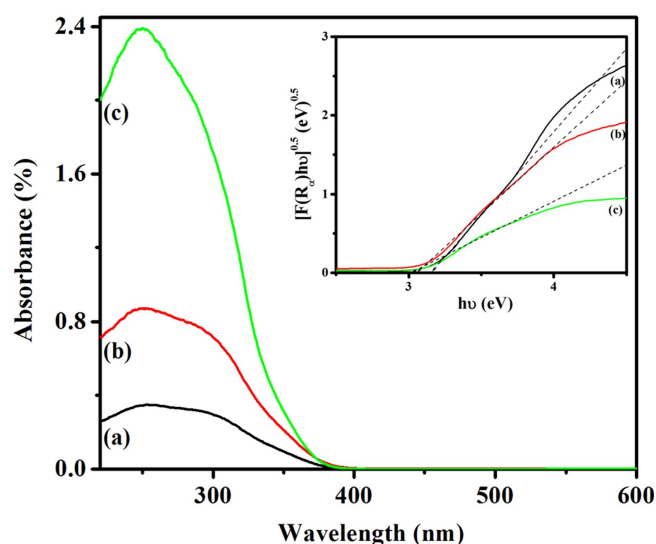**Figure 3.** Particle size distribution for TiO_2 nanoparticles of (a) S_1 (b) S_2 and (c) S_3

Figure 4. Absorbance spectra for TiO_2 nanoparticles of (a) S_1 (b) S_2 and (c) S_3 and inset shows the band gap spectra using Kubelka-Munk function

Figure 5. Photoluminescence spectra of TiO_2 nanoparticles of (a) S_1 (b) S_2 and (c) S_3
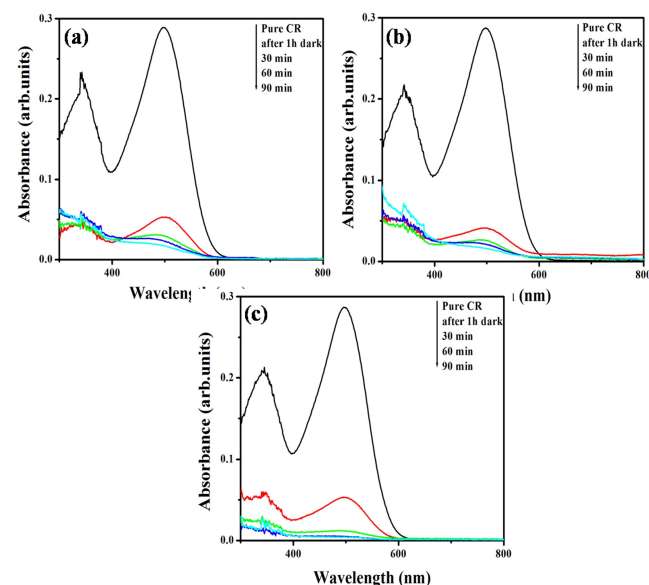
Figure 6. Degradation of Congo red using TiO2 nanoparticles of TiO_2 nanoparticles of (a) S_1 (b) S_2 and (c) S_3

3.3 Removal of Congo red

Congo red was chosen as a model pollutant with a concentration of 10 ppm. 10 mg of TiO_2 was dispersed in 50 ml of CR solution. The solution was magnetically stirred in the dark for 60 min to achieve the adsorption desorption equilibrium between the dye and catalyst. In dark, the degradation of the dye solution was attributed to the adsorption of congo red on the surface of TiO_2 nanoparticles through two oxygen atoms in the sulphonate group present in the dye. Although CR is an anionic dye, the photodegradation originated from the hydroxyl and superoxide anion radicals resulting from the formation of electron-hole pairs in semiconductors. When TiO_2 is exposed using xenon source, electrons in the valence band are excited to the conduction band leaving behind holes.
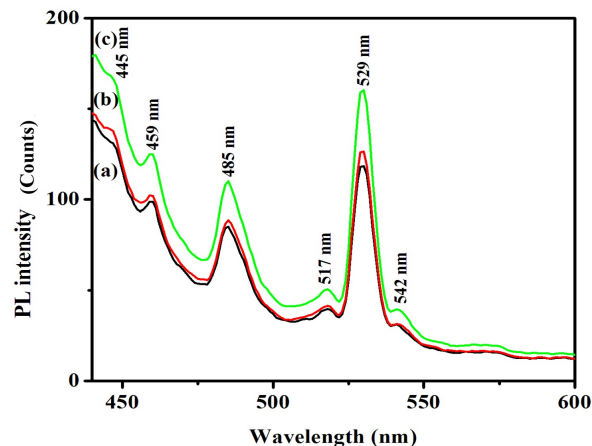
The excited electrons in the conduction band are in a 3d state and because of dissimilar parity, the transition probability of e^- to the valence band decreases, leading to a reduction in the electron-hole recombination [19]. The absorbance spectra of CR shown in figure 6 have two characteristic peaks are in the visible region at 498 nm and the other band at 338 nm and are due to the azo bond (-N=N-) and naphthalene ring structure of CR dye [20] respectively.

During degradation the absorbance value decreases with irradiation time and it is due to the breakup of chromophore bonds in CR dye. With the increase in the hydrothermal temperature, a maximum degradation efficiency of 98.3 % is achieved in 90 min. This improvement may be attributed to the perfect crystal structure of TiO_2 [21].

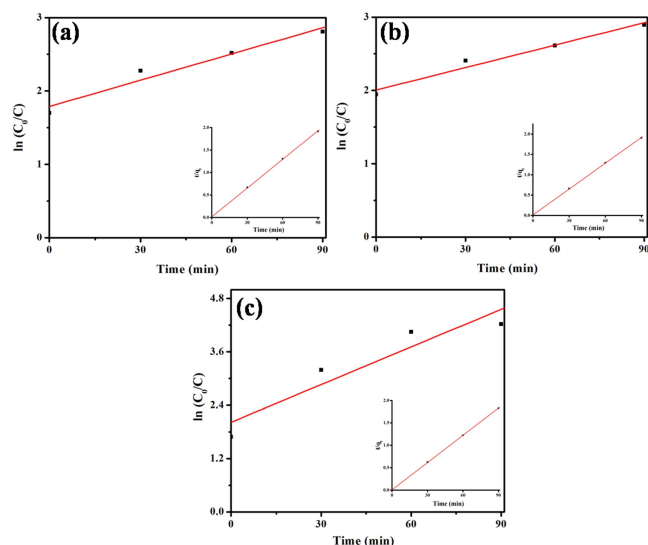The absorption spectra reveal the decrease of dye concentra-

Figure 7. Langmuir-Hinshelwood pseudo first order kinetics for the degradation of CR using TiO$_2$ nanoparticles of (a) S$_1$ (b) S$_2$ and (c) S$_3$ and the inset figure shows the second order kinetics

Figure 8. XRD pattern for TiO$_2$ nanoparticles of (a) S$_1$ (b) S$_2$ and (c) S$_3$

tion with time for all the samples and the sample S$_3$ shows the maximum degradation efficiency in 90 min. The amount of dye adsorbed per unit (q$_e$) was calculated using the following equation

$$q_e = \frac{V(C_i - C_f)}{m} \tag{2}$$

where V is the volume of the dye solution (ml), C$_i$ and C$_f$ are the initial and final concentration (mg l^{-1}) of the dye respectively and m is the weight of the catalyst (g). The q$_e$ value obtained from the experiment is given in Table 1. The degradation of CR dye by TiO$_2$ nanoparticles are analyzed using pseudo first order and pseudo second order kinetics.

4. Kinetics of CR dye removal

4.1 Pseudo first order kinetics

The kinetics of photocatalytic degradation is described using Langmuir– Hinshelwood model. When the initial concentration C$_0$ is very small then the equation is expressed as [22]

$$\ln\left(\frac{C_0}{C_t}\right) = kt \tag{3}$$

where k $\rightarrow$ pseudo first order rate constant and C$_t$ is the concentration at time t. The variation in $\ln\left(\frac{C_0}{C_t}\right)$ as a function of time is shown in figure 7.

The removal efficiency, first order kinetic rate constant (k) and regression coefficient (R) are given in Table 1. Since, the regression coefficient is not nearly equal to unity, in the present work, pseudo second order kinetics are tried.
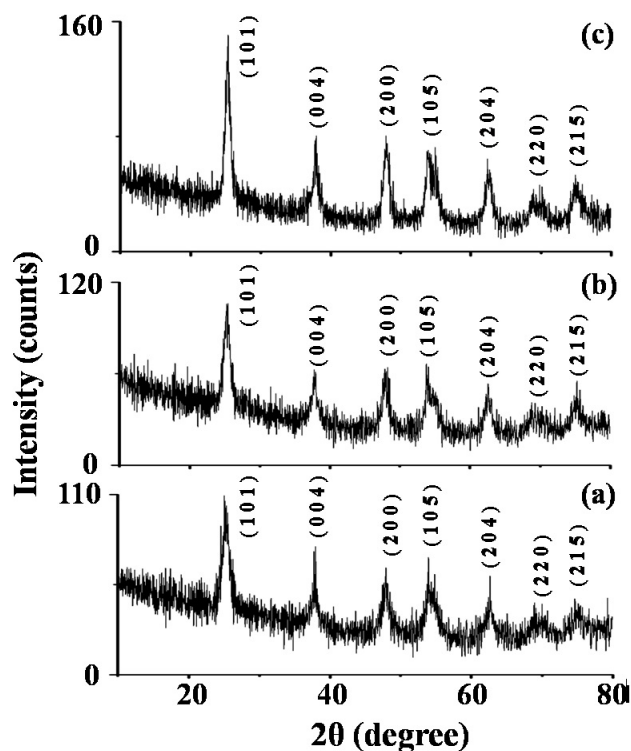
Blanchard [23] presented the pseudo second order as,

$$q_t = \frac{k_2 q_e^2 t}{1 + k_t q_e t} \tag{4}$$

where q$_e$ and q$_t$ are the amount of dye adsorbed at equilibrium and at time t (mg/g) and k$_2$ is the pseudo second order rate constant (g mg^{-1} min^{-1}). The obtained equation can be rearranged into a linear form as,

$$\frac{t}{q_t} = \frac{t}{q_e} + \frac{1}{k_2 q_e^2} \tag{5}$$

A plot between t/q$_t$ versus time (inset of figure 7) gives the value of qe (mg/g) and k$_2$ (g mg^{-1} min^{-1}) and given in Table 1 for comparison. The regression coefficient values are nearly equal to 1 and it exhibits the pseudo second order fitting.
The stability of TiO$_2$ is tested by studying the structural change (XRD) of the sample after degradation. Figure 8 shows the XRD pattern of all the three samples after degradation of CR. It should be noted that only anatase peaks can be detected and no rutile or brookite phase is found in the XRD pattern. All the X-ray diffraction peaks match well to anatase phase of TiO$_2$ and the peaks are in agreement with the reference pattern JCPDS No. 71-1167 of TiO$_2$. From this it is clearly confirmed that, the formed system crystallizes in tetragonal structure. No additional peaks are present after degradation but the XRD intensity decreases slightly. It shows that the crystal structure remains the same after degradation,

Table 1. Pseudo first & second order kinetics parameters of TiO_2 for the degradation of CR dye

Sample	Efficiency (%)	q_e (mg/g) (from experiment)	First order k_1 (min^{-1})	R	q_e (mg/g) (from graph)	Second order k_1 (min^{-1})	R
S_1	92.7	46.99	0.012(1)	0.9790	47.01	0.0302	0.9997
S_2	93.7	47.23	0.010(1)	0.9854	47.23	0.0367	0.9998
S_3	98.3	49.26	0.028(7)	0.9436	49.38	0.0579	0.9999

but the crystallinity decreases. The crystallite size (D) of TiO_2 is calculated using the Scherrer formula given by,

$$D = \frac{K\lambda}{\beta \cos\theta} \quad (6)$$

where $K \rightarrow$ Scherrer constant (= 0.9), $\lambda \rightarrow$ wavelength of X-ray used, $\beta \rightarrow$ full width at half maximum and $\theta \rightarrow$ scattering angle. The crystallite size is determined by considering the first three prominent peaks and its average value is 6.3, 7.6 and 13.6 nm for sample S_1, S_2 and S_3 respectively.

The observed crystallite size increase with decrease in the band gap, have a direct relation of increase in degradation efficiency. The efficiency increases with hydrothermal temperature and S_3 shows the highest efficiency for CR. Due to the lower band gap of sample S_3, the number of electrons reaching the conduction band from valence band increases (i.e.,) electron density in the conduction band is high. Consequently, the number of holes in the valence band also increases. Both these electrons and holes interact with OH^- to produce OH^o radicals. This favors the formation of more OH^o free radicals, which are main active species in the photocatalytic degradation [24]. These results revealed that the larger crystallite size and the lower band gap of sample S_3 shows highest efficiency compared to other samples.

5. Conclusion

Anatase TiO_2 nanoparticles are prepared successfully by a hydrothermal method by varying the hydrothermal temperatures. With the increase in hydrothermal temperature, the crystallinity increases while the band gap, surface defects and charge carrier recombination rate decreases. A maximum degradation efficiency of 98 % is achieved in 90 min on the CR dye removal. The significant enhancement in the degradation of sample hydrothermally treated at 160 ^{o}C, is due to the lower recombination rate, anatase phase with a higher degree of crystallinity and the lower band gap of TiO_2 nanoparticles.

References

[1] M. Anpo. *Pure Appl.Chem.*, **72**:1265, 2000.

[2] Y.K. Abdel-Monem. *J. Mater. Sci: Mater. Electron.*, **27**:5723, 2016.

[3] N.V. Lebukhova, N.F. Karpovich, S.A. Pyachin, E.A. Kirichenko, K.S. Makarevich, and M.A. Pugachevskii. *Theor. Found. Chem. Eng.*, **51**:820, 2017.

[4] A. Karami. *J. Iran. Chem. Soc.*, **7**:S154, 2010.

[5] H. Guo, K. Lin, Z. Zheng, F. Xiao, and S. Li. *Dyes and Pigments.*, **92**:1278, 2012.

[6] M. Farbod and M. Khademalrasool. *Powder Technol.*, **214**:344, 2011.

[7] M.L. De Souza, D.C. Tristao, and P. Corio. *RSC Adv.*, **4**:23351, 2014.

[8] m. Malligavathy, S. Iyyapushpam, S.T. Nishanthi, and D.Pathinettam Padiyan. *Pramana*, **90**:44, 2017.

[9] L. Yang and B. Kruse. *J. Opt. Soc. Am. A.*, **21**:1933, 2004.

[10] J. Wang, P. Zhang, X. Li, J. Zhu, and H. Li. *Appl. Catal B: Environ.*, **134**:198, 2013.

[11] Q. Xiang, T. Yu, and P.K. Wong. *J. Colloid. Interface Sci.*, **357**:163, 2011.

[12] Y. Lei and L.D. Zhang. *J. Mater. Res.*, **16**:1138, 2001.

[13] J.G. Yu, T.T. Ma, and S.W. Liu. *Phys. Chem. Chem. Phys.*, **13**:3491, 2011.

[14] H.G. Roy. *Int. J. Mater. Sci Innov.*, **1**:142, 2013.

[15] J.G. Yu, L. Yue, S.W. Liu, B.B. Huang, and X.Y. Zhang. *J. Colloid Interface Sci.*, **334**:58, 2009.

[16] Y.X. Zhang, G.H. Li, Y.X. Jin, Y. Zhang, J. Zhang, and L.D. Zhang. *Chem. Phys. Lett.*, **365**:300, 2002.

[17] B. Santara. and P.K. Giri. *Mater. Chem. Phys.*, **137**:928, 2013.

[18] K.P. Priyanka, S. Joseph, A.T. Sunny, and T. Varghese. *Nanosystems: Physics, Chemistry, Mathematics*, **4**:218, 2013.

[19] S. Banerjee, J. Gopal, and P. Muraleedharan. *Current Sci.*, **90**:1378, 2006.

[20] J. Wang, R.H. Li, Z.H. Zhang, W. Sun, R. Xu, Y.P. Xie, Z.Q. Xing, and X.D. Zhang. *Appl. Catal., A: General.*, **334**:227, 2008.

[21] M. Xue, L. Huang, J.Q. Wang, Y. Wang, L.Gao, J.H. Zhu, and Z.G. Zou. *Nanotech.*, **19**:185604, 2008.

[22] D.W. Chen and A.K. Ray. *Wat. Res.*, **32**:3223, 1998.

[23] G. Blanchard, M. Maunaye, and G. Martin. *Water Res.*, **18**:1501, 1984.

[24] S. Horikoshi, A. Saitou, H. Hidaka, and N. Serpone. *Environ.Sci.Technol.*, **37**:5813, 2003.